Detection and Reconstruction of Gravitational Waves from Core-Collapse Supernovae

A Thesis

submitted to
Indian Institute of Science Education and Research Pune
in partial fulfillment of the requirements for the
BS-MS Dual Degree Programme

by

Anushka Doke

Indian Institute of Science Education and Research Pune
Dr. Homi Bhabha Road,
Pashan, Pune 411008, INDIA.

May, 2023

Supervisor: Dr. Elena Cuoco

Certificate

This is to certify that this dissertation entitled **Detection and Reconstruction of Gravitational Waves from Core-Collapse Supernovae** towards the partial fulfilment of the BS-MS dual degree programme at the Indian Institute of Science Education and Research, Pune represents study/work carried out by Anushka Doke at the Indian Institute of Science Education and Research, Pune and Scuola Normale Superiore under the supervision of Dr. Elena Cuoco, Head of European Gravitational Observatory Data Science Office and Associate Faculty at Scuola Normale Superiore, during the academic year 2022-2023.

Anushka Doke

Dr. Elena Cuoco

Committee:

Dr. Elena Cuoco

Prof. Ramana Athreya

The most exciting phrase to hear in science, the one that heralds new discoveries, is not "Eureka!" but "That's funny…"

— Isaac Asimov

Declaration

I hereby declare that the matter embodied in the report entitled **Detection and Reconstruction of Gravitational Waves from Core-Collapse Supernovae** are the results of the work carried out by me at the Indian Institute of Science Education and Research, Pune and Scuola Normale Superiore under the supervision of Dr. Elena Cuoco and the same has not been submitted elsewhere for any other degree.

Dr. Elena Cuoco

Anushka Doke

Acknowledgements

I would like to express my sincere gratitude to my supervisor Dr. Elena Cuoco for her unwavering support throughout my thesis. She was always there to answer my questions, provide feedback, and help me navigate the challenges that came my way. Her extensive knowledge and expertise in the field of research were invaluable, and I have learned so much from her. I would also like to extend my appreciation to Prof. Ramana Athreya for providing me with insightful comments on my thesis work. Prof. Sourabh Dube has been my mentor during the past four years at IISER, and I cannot thank him enough for his invaluable guidance. He introduced me to research in the fields of physics and machine learning. Under his mentorship, I developed a research-oriented mindset, which proved to be instrumental in completing my master's project successfully. Completing my thesis would not have been possible without the support and guidance of Alberto, and I would like to express my heartfelt gratitude to him. Our countless hours of discussions and brainstorming sessions helped me develop a more scientific and analytical approach. His willingness to help me overcome any obstacles I encountered throughout the process was truly invaluable. I would also like to thank Francesco and Alessandro for their valuable inputs during the weekly group meetings.

I am deeply grateful to Dr. Jade Powell for providing the waveforms used in this study. I thank Scuola Normale Superiore (SNS) for accepting me as a project student and granting me access to their VPN services and their supercomputer Hal. Access to Hal was critical to my research, and I thank the IT department at IISER Pune for enabling me to access the VPN at SNS. I would also like to acknowledge the financial support that I have received from the DST-INSPIRE Scholarship for Higher Education throughout my undergraduate studies. Lastly, I am grateful to the Physics Department at IISER Pune for providing me with this opportunity.

I would like to thank my friends, who became a family away from home for me. And thank you, Aai and Baba, for your unconditional support and encouragement.

Abstract

Since their first detection by the Advanced LIGO interferometers, GW150914, gravitational waves have provided unique scientific insight into high-energy astrophysical events, such as compact binary mergers involving black holes and neutron stars. Core-collapse supernovae are among the types of signals that have eluded detection thus far, and a significant effort is therefore being put into achieving a detection in coming years. Compared to binary mergers, core-collapse supernovae cannot be modelled precisely, and it is, therefore, impossible to apply classical matched filter techniques for detection and analysis. In order to gain valuable information from this type of event, a correct estimate of the source parameters has to be obtained, such as the mass and radius. Parameter estimation heavily relies on a critical aspect of gravitational wave data analysis: signal reconstruction. In this thesis project, we efficiently detected and reconstructed gravitational wave signals embedded in the typical noise background of the Einstein Telescope. Specifically, we focused on the use of wavelet-based algorithms, which have been successfully applied for signal reconstruction in many fields. We first detected and clustered the triggers from simulated core-collapse supernovae gravitational wave events and then reconstructed the signals. For the background, we used simulated Gaussian noise built from the estimated sensitivity curve of the Einstein Telescope. We employed gravitational waveforms obtained from modern 3D simulations to model core-collapse supernovae signals.

Contents

List of Figures

List of Tables

Introduction

Gravitational waves (GWs) are ripples in the fabric of spacetime that propagate through the universe at the speed of light. First predicted by Albert Einstein in 1916 as a consequence of his theory of general relativity, it was not until a century later that the first direct detection of GWs was achieved by the Laser Interferometer Gravitational-Wave Observatory (LIGO) Collaboration and the Virgo Collaboration in 2015 [1]. The discovery of GW150914, a signal produced by the merger of two black holes, marked the beginning of a new era in astrophysics, offering a unique window into the most energetic and violent events in the universe. The initial three observing runs (O1, O2 and O3) have yielded a plethora of GW detections [2–4]. We expect a considerable increase in the number of detections with future enhancements to these detectors and with the addition of third-generation GW interferometers - the Einstein Telescope (ET) and the Cosmic Explorer (CE) - to the global detector network. To date, all the detections have been from compact binary systems. We anticipate the detection of burst signals from the upcoming observing runs. The most prominent are the signals from core-collapse supernovae (CCSNe).

Core-collapse supernovae are violent explosive events that mark the endpoint of the lives of massive stars, and are crucial for the evolution of the universe. They produce neutron stars and black holes, and disseminate newly synthesized elements into the interstellar medium, affecting star formation and evolution. Despite significant research progress, there are still many unanswered questions about CCSNe. When the core collapses to form a protoneutron star (PNS), a massive amount of gravitational binding energy is released, mainly carried away by neutrinos. Only a small proportion of this energy is converted to the kinetic energy of the explosion. Aspherical flows are generated in the star's central region, producing strong gravitational waves. An electromagnetic (EM) burst is emitted from the outer edge of the star hours later, containing limited information about the CCSN central engine's inner regions. However, gravitational waves, generated by aspherical motion in the central core, carry information about the central engine's dynamics, while neutrinos

carry information about the thermodynamic conditions at the surface of the protoneutron star [5].

Observations of gravitational waves and neutrinos can provide insight into the CCSN central engine and the explosion mechanism, revealing information about the innermost regions of the star's rotation and structure. Unfortunately, gravitational waves from CCSNe have yet to be detected, and the aLIGO-VIRGO network's sensitivity range is limited to a few kiloparsecs. Additionally, the low CCSNe rates within galaxies reduce the probability of detecting gravitational waves from CCSNe. The ET's sensitivity range, however, will extend up to our galactic neighbourhood [6].

Given the chaotic phenomena in a CCSN, such as turbulent convection, which adds stochasticity to the GWs generated, deterministic search methods like matched-filtering cannot be used. The search algorithms employed to detect GW signals from CCSNe must use weak or minimal assumptions. These algorithms should be equipped to handle a wide range of GW morphologies, including unexpected ones. In this project, we use a novel algorithm called the Wavelet Detection Filter (WDF). It is a wavelet-based detection pipeline and is agnostic to the signal models. Because of the many different kinds of wavelets used, it can analyze both long and short signals with a variety of morphologies. We perform an analysis of simulated state-of-the-art CCSNe models and test the detection and reconstruction accuracies of WDF for the Einstein Telescope.

The outline of the thesis is as follows: Chapter 1 provides a short introduction to the theory of gravitational waves, current ground-based detectors, and future detectors, including their noise sources. This chapter will also discuss the sources of gravitational waves, with an extensive focus on core-collapse supernovae and the types of explosion mechanisms that give rise to them. Chapter 2 outlines the tools and techniques used in this study, including the data used, data processing steps, the event generation pipeline, and the clustering of triggers. This chapter describes how the wavelet-based algorithm is employed to detect and reconstruct signals in the Einstein Telescope's background noise. Chapter 3 presents the results obtained from clustering and reconstruction, as well as a detailed discussion of these results. Finally, Chapter 4 summarises the findings from this work and discusses their implications for future scientific research. This chapter provides an outlook on future work in this area, highlighting the potential of wavelet-based algorithms for the detection and reconstruction of gravitational wave signals from core-collapse supernovae.

Chapter 1

Background and Theory

A long time ago in a galaxy far, far away, two black holes merged into one, and in 2015, the LIGO and Virgo Scientific Collaborations detected the gravitational waves from that event. It marked a new era in astrophysics and garnered significant interest from the scientific community and the public alike. Since then, gravitational waves have emerged as a promising tool for multi-messenger astronomy, providing a wealth of information about the astrophysical phenomena that produce them. With the development of more sensitive detectors, the frequency of gravitational wave detections is expected to increase significantly in the coming years. This will enable researchers to explore a wide range of astrophysical processes and phenomena, from the collisions of massive black holes to the violent explosions of supernovae. In this chapter, we provide an overview of gravitational waves, their detection, and their potential for advancing our understanding of the universe.

1.1 The Physics of Gravitational Waves

Einstein predicted gravitational waves as a solution to the linearized theory of gravity. Linearized gravity is a perturbation of the Minkowski spacetime. As described in [7], Einstein's field equations are given by

$$R_{\mu\nu} - \frac{1}{2}\, g_{\mu\nu}\, R + \Lambda\, g_{\mu\nu} = \frac{8\pi G}{c^4}\, T_{\mu\nu} \tag{1.1}$$

where $R_{\mu\nu}$ is the Ricci tensor, R is the Ricci scalar, $g_{\mu\nu}$ is the spacetime metric tensor, Λ is the cosmological constant describing the dark energy component, and $T_{\mu\nu}$ is the stress tensor. Here

assume

$$g_{\mu\nu} = \eta_{\mu\nu} + \epsilon h_{\mu\nu} \tag{1.2}$$

where $0 < \epsilon \ll 1$. The perturbation $\epsilon h_{\mu\nu}$ is therefore assumed to be small.

Developing the left-hand side of equation 1.1 in powers of ϵ and neglecting all terms involving ϵ^k with $k > 1$, the linearized Einstein field equations can be written with the following definition:

$$\bar{h}_{\mu\nu} = h_{\mu\nu} - \frac{1}{2}\eta_{\mu\nu}h_{\alpha\beta}\eta^{\alpha\beta} \tag{1.3}$$

as

$$\Box\bar{h}_{\mu\nu} = -\frac{16\pi G}{c^4}T_{\mu\nu}, \qquad \Box = \eta_{\mu\nu}\partial^{\mu}\partial^{\nu} \tag{1.4}$$

This is the gravitational wave equation in flat spacetime. In order to describe the rate at which gravitational waves are emitted from a system, the quadrupole formula is used. The formula reads

$$\bar{h}_{ij}(t, \mathbf{x}) = \frac{2G}{c^4 r}\ddot{I}_{ij}(t - r/c) \tag{1.5}$$

where $\bar{h}_{ij}(t.r)$ is the spatial part of the trace reversed perturbation of the metric, i.e. the gravitational wave, G is the gravitational constant, c the speed of light in vacuum, and I_{ij} is the mass quadrupole moment [8]. The quadrupole moment is given by

$$I_{ij} = \int \rho(t, \mathbf{x})(x_i x_j - \frac{1}{3}r^2\delta_{ij})\, d^3x \tag{1.6}$$

where $|\mathbf{x} - \mathbf{x}'| = r, \quad t - r/c$ is the retarded time, ρ is the mass density, and x_i is the position vector of one of the masses. There is no monopole and dipole gravitational radiation because of the conservation of mass and total momentum, respectively. As expressed in Equation 1.5, gravitational waves are emitted solely when there is a non-zero second derivative of the quadrupole moment. Despite the fact that the GW amplitude falls off as $\frac{1}{r}$, the pre-factor $\frac{G}{c^4} \sim 8.26 \times 10^{-45}$ means that even a dense asymmetric distribution will produce a relatively weak signal. The waves detectable from Earth have $h \sim 10^{-21}$. The types of sources we can detect from Earth are discussed in Section 1.3.

1.2 Signal Processing Techniques for Gravitational Waves

1.2.1 Time Series

A stochastic process is a collection of random variables X_t indexed by a set T, i.e. $t \in T$. If T consists of integers or a subset of integers, and if the values taken on by this process are real, it is called a time series. GW detectors record data in the form of time series. Each detector collects data at a specific sampling frequency f_s, which represents the number of data points collected per second.

1.2.2 Autoregressive Model

The autoregressive (AR) model is a time series model that employs past data points to predict future observations. An AR(p) model specifically utilizes past values, or lags, denoted by $y(t)$, to anticipate future values. The parameter 'p' represents the order of the AR model. A first-order AR model would be denoted as AR(1). The outcome variable in a first-order AR process at a given point in time t is linked solely to time periods that are one interval apart, represented by the variable's value at $t-1$. In contrast, an AR model of higher order, such as second or third-order AR processes, would incorporate data points separated by two or three intervals, respectively [9].

An AR(p) model is defined as:

$$y(t) = \delta + \phi_1 y(t-1) + \phi_2 y(t-2) + \ldots + \phi_p y(t-p) + \epsilon(t) \tag{1.7}$$

where

- ϕ_i are the parameters of the model
- $\delta = (1 - \sum_{i=1}^{p} \phi_i)\,\mu$, where μ is the mean
- $y(t-1), y(t-2), \ldots, y(t-p)$ are the lags (past values of y)
- $\epsilon(t)$ is white noise (randomness)

This analysis uses an AR model of order 2000, i.e., an AR(2000) model. It is used to model the power spectral density of the noise. This model is then employed in the process of whitening the data.

1.2.3 Amplitude Spectral Density

The detector noise is typically characterized by its power spectral density (PSD). The power spectral density for a stationary random process $x(t)$ is given by

$$S_x(f) = \lim_{T\to\infty} \frac{1}{T} |\hat{x}_T(f)|^2 \tag{1.8}$$

where $\hat{x}(f)$ is the Fourier transform of $x(t)$ represents the time series. It is obtained through the Fourier transform of the autocorrelation function and depicts the distribution of power as a function of frequency per unit frequency. The square root of PSD is the amplitude spectral density (ASD), which is also used for noise description. It has the units of $\mathrm{Hz}^{-1/2}$.

1.3 Ground-based Interferometers for the Detection of Gravitational Waves

1.3.1 Michelson-Morley Interferometer

The current ground-based detectors - the two LIGO detectors, Virgo, KAGRA and GEO600 - are all Michelson interferometers. The Michelson interferometer has two arms at 90 degrees. The arms of Virgo are 3 km long, while the arms of LIGO are 4 km long. The longer the arms of an interferometer, the more sensitive it is to gravitational-wave measurements. A 3-4 km interferometer is still not sensitive enough to detect gravitational waves. To detect a gravitational wave with frequency f_{GW}, the ideal length of the arm of a Michelson interferometer is given by [10]

$$L = 750\,\mathrm{km}\left(\frac{100\,\mathrm{Hz}}{f_{GW}}\right) \tag{1.9}$$

This is resolved by using Fabry-Perot Cavities. Additional mirrors are placed in both arms near

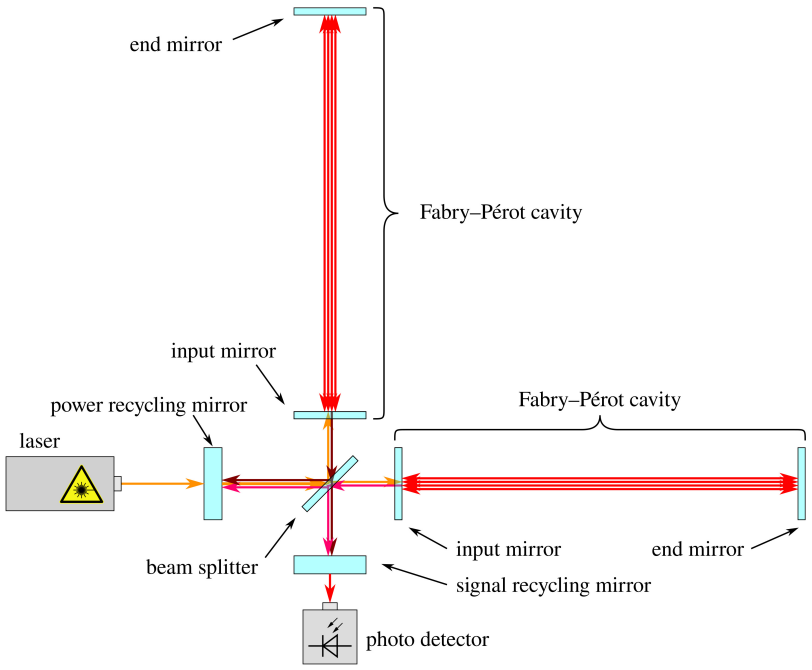

Figure 1.1: A schematic of the LIGO detector (source: LIGO. (2021, December 23). In Wikipedia.)

the beam-splitter. The beam bounces around in each of the 4 km arms about 300 times before combining with the beam from the other arm. So the effective distance travelled by each laser increases from 4 km to 1200 km.

In the interferometer, light is divided with equal probability amplitude into the two arms using the beam splitter. It travels through the arms, bounces around a few times, and finally crosses the beam splitter again, where the two beams merge into one. The phase difference between the two beams is measured depending on the interference pattern observed at the photodetector.

Gravitational waves stretch and squeeze spacetime as they travel through it. When a gravitational wave passes through a detector, one arm gets longer while the other gets shorter, and vice-versa, and it continues till the wave passes. This results in a net difference in the total distance the laser travels in the two arms.

$$\frac{\delta L}{L} = h \tag{1.10}$$

It can be seen from this equation that the amplitude of the gravitational waves h is proportional to the net difference in the length of the two arms.

1.3.2 Noise Sources

The performance of the interferometric detectors is limited by the various noise sources that can affect their sensitivity. Some of the most important noise sources are as follows:

- **Seismic noise:** This includes all the processes, such as winds, earthquakes, and anthropogenic activities, which shake the detector components. It is the dominant noise contribution below ~10 Hz. The amplitude spectral density of seismic noise depends on the frequency f and the location through a factor B as [10]:

$$\sqrt{S_x(f)} = B\left(\frac{1Hz}{f^{\nu}}\right) \mathrm{m} \cdot \mathrm{Hz}^{-1/2} \tag{1.11}$$

  For a particularly quiet place, $B \sim 10^{-7}$ and the power law index $\nu \simeq 2$ [10]. Seismic noise is mitigated using a superattenuator. The superattenuator is a five-stage pendulum supported by three legs connected to the ground, called the inverted pendulum. This helps suppress the transmission of ground seismic vibrations to the suspended mirror [11]. This method attenuates the seismic noise below a level interesting for GW detection only at frequencies >10 Hz. This is the main reason why ground-based interferometers cannot detect GWs below ~10 Hz [10].

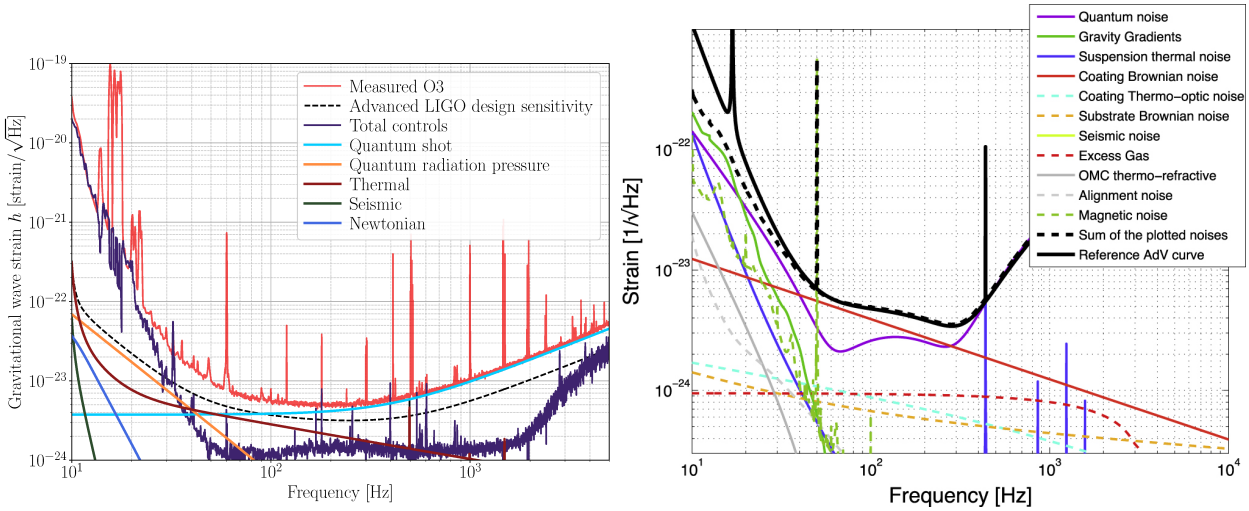

(a) O3 Ligo Hanford noise budget [12]

(b) Advanced Virgo noise budget [13]

Figure 1.2: The most important noise contributions affecting the sensitivity of the Advanced LIGO and the Advanced Virgo detectors in the form of amplitude spectral density (ASD) vs frequency.

- **Newtonian noise:** Also known as 'gravity gradient noise', this is caused by any kind of change in the gravitational potential around the optics. It is generated by the fluctuating gravitational forces in the nearby region. It is not the dominant noise effect in the current ground-based interferometers. It is dominated by the seismic noise below a few Hz and the thermal noise above a few Hz [10].

- **Thermal noise:** It includes the processes that induce vibrations in the test masses and the suspensions. This includes the noise associated with the suspension mechanism, the oscillations of atoms of the mirror due to their kinetic energy, and temperature fluctuations in the mirror surfaces at the point where the laser impinges. The following are the most relevant thermal noise sources:

  - Suspension thermal noise: This component is associated with the inverted pendulum that we discussed before. The pendulum modes generate a horizontal displacement from the swinging motion due to thermal fluctuations. It affects the sensitivity in the range from a few Hz to ~50 Hz. Violin modes are the excitations of the normal modes of the wire attached to the payload. In the sensitivity curve of the detector, they are responsible for the set of spikes between 300 Hz and a few kHz.
  - Coating Brownian noise: At a given temperature, the atoms comprising a mirror have a certain kinetic energy due to their motion. This produces the mirror thermal noise. It is predominant in the region between tens of Hz to a few hundred Hz.

- **Quantum noise:** The main fundamental limit to the detector sensitivity is posed by the vacuum electric field fluctuations at the interferometer readout port. Quantum noise manifests as shot noise and quantum radiation pressure noise [12]. The high-frequency contribution is the shot noise, which is produced due to the fluctuations in the number of photons that reach the photodetector during an interval T. It affects the sensitivity at hundreds of Hz. The low-frequency contribution is the radiation pressure, caused by the momentum transfer of photons when they impinge on the mirrors and get reflected back. Beyond a certain limiting value (a few tens of Hz), radiation pressure becomes more important and dominates over shot noise (Figure 1.2). The quantum noise at a given frequency can be decreased by using heavier test masses or longer arm lengths [10]. Also, squeezed light can be used instead of the output laser light to decrease the noise strain sensitivity in the high-frequency region ($f > 200$ Hz) [14, 15].

The contributions of some of these sources to the noise budgets of the O3 LIGO Hanford detector

and the Advanced Virgo detector are summarized in Figure 1.2 in terms of their ASD content. At low frequencies (below 10 Hz), the sensitivity curve is dominated by Newtonian and seismic noise, at mid-frequencies by different thermal noise contributions (mirror coating Brownian noise, for instance) and at higher frequencies (hundreds of Hz) by quantum shot noise.

Transient Noise and Long-Lived Disturbances

Transient noises include all those sources which are short-lived and thus affect the sensitivity of the detector only for a short period of time. Glitches are generally transient noises with $\Delta t \lesssim 1s$. See Figure 1.3 for an example of a glitch. Such a glitch, overlapping with a GW event, can adversely affect its detection. Glitches might affect and trigger pipelines which make no assumptions about

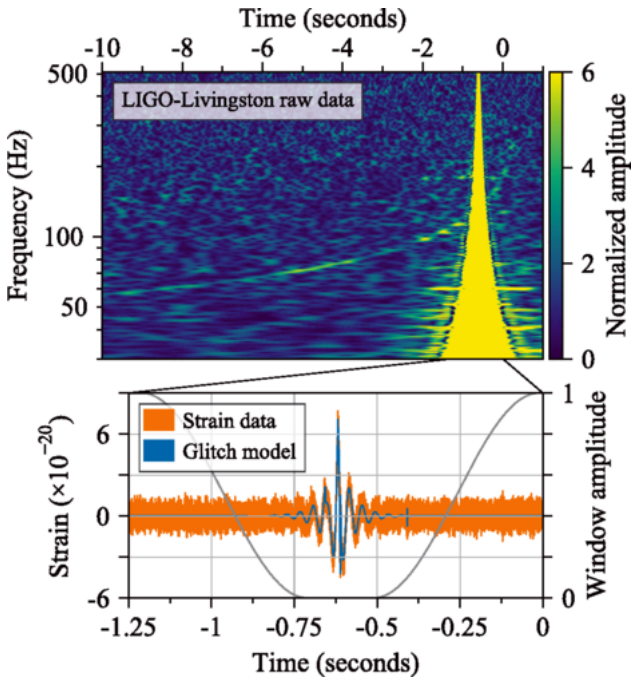

Figure 1.3: An example of a glitch in LIGO-Livingston data used in the initial identification of GW170817. The top panel shows a time-frequency representation of the raw LIGO-Livingston data, while the bottom panel displays the glitch in the time domain. The gravitational-wave strain amplitude of GW170817 is of the order of 10^{-22} and so is not visible in the bottom panel [16].

the gravitational wave signal model, such as the burst pipelines. Moreover, strong glitches may produce saturation effects in the interferometer monitoring channels and trigger vetoes on the data and thus need to be removed [16].

Glitch classification and characterization are important to eliminate these artifacts, thereby

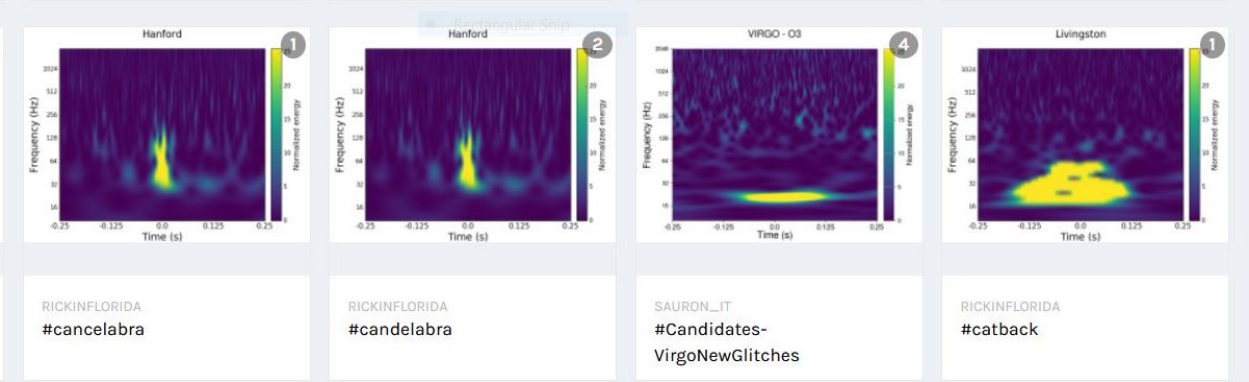

Figure 1.4: Glitches present in data from the LIGO Hanford, LIGO Livingston and Virgo detectors from the Gravity Spy gallery [17].

improving the detection of astrophysical signals. Initiatives such as Gravity-Spy and GWitch Hunters maintain a repository of glitches from data recorded at the LIGO Hanford, LIGO Livingston and Virgo detectors (see Figure 1.4) [17, 18]. Citizen scientists contribute by looking through segments of data and classifying these glitches. This will then be used to train machine learning algorithms to identify and isolate glitches.

Conversely, long-lived disturbances persist over a considerable duration. These disturbances might affect the sensitivity of continuous wave searches. Long-lived disturbances affect the ASD estimation and whitening procedures (see Chapter 2) since they contribute to the stationary part of the ASD. Loud glitches can also affect the ASD estimation in some segments of data. Typically, it is good practice to compute the ASD used for whitening in the absence of such transients.

1.3.3 Current and Future Detector Capabilities

This section summarises the observing runs of the advanced detectors till now. Figure 1.5 shows the timeline of the past and future runs, along with the sensitivities reached and planned, respectively.

During observing run O1, Virgo was undergoing an upgrade. KAGRA in Japan joined at the end of the third run (O3). LIGO-India is expected to join the network of detectors from O5. The first observing run (O1) took place from September 2015 to January 2016. The first gravitational wave event was observed during this run. The second run (O2) took place from November 2016 to August 2017 after upgrading the detectors. Advanced Virgo joined O2 in August 2017. The

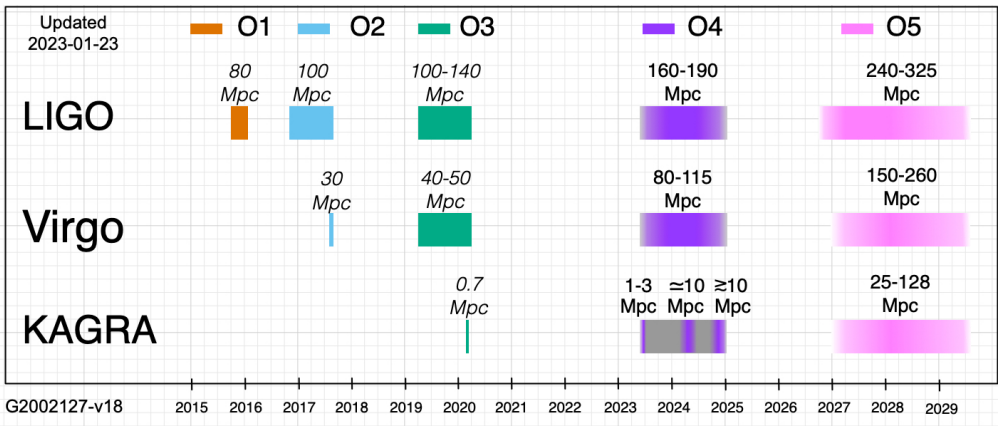

Figure 1.5: Past and upcoming observing runs for the advanced gravitational wave detectors [19].

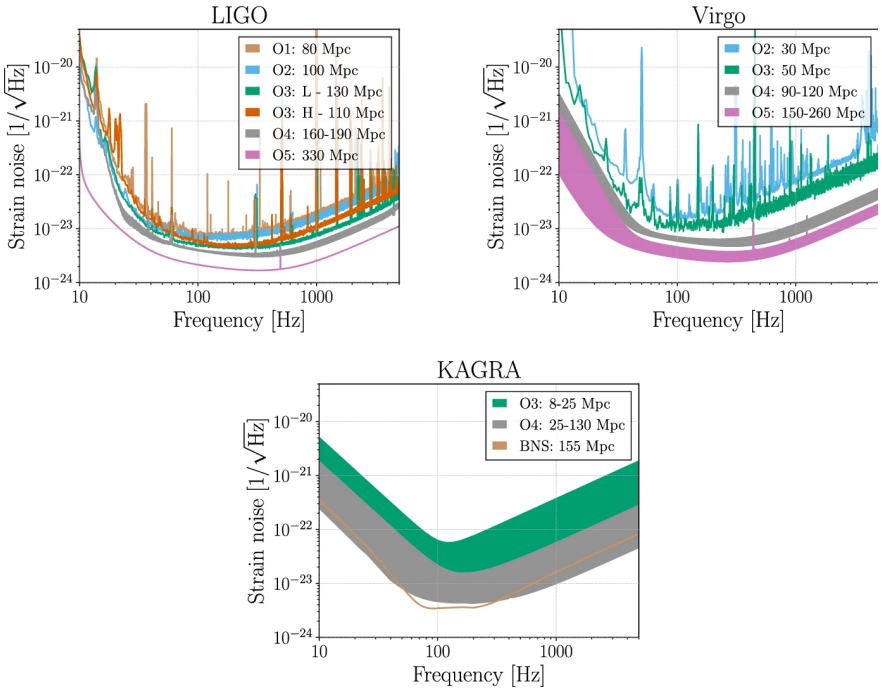

Figure 1.6: Past and planned future sensitivity improvements for LIGO, Virgo and KAGRA [19].

analysis of O1 and O2 data produced 11 confident detections (10 binary black hole mergers and one binary neutron star merger) and 14 marginal triggers [20]. These events have been described in the first Gravitational-Wave Transient Catalog (GWTC) by the LIGO Scientific Collaboration and the Virgo Collaboration [2].

Advanced LIGO and Advanced Virgo initiated their third observing run (O3) in April 2019, which ended in March 2020. It was divided into two parts - O3a and O3b - with a break between

October 1, 2019, and November 1, 2019. There are 56 detection candidates at the time of writing, as reported in the Gravitational-Wave Candidate Event Database (GraceDB) [21]. The candidate events observed during O3a are reported in GWTC-2 [3]. During O3b, 35 detection candidates have been identified. These events have been reported in GWTC-3 [4].

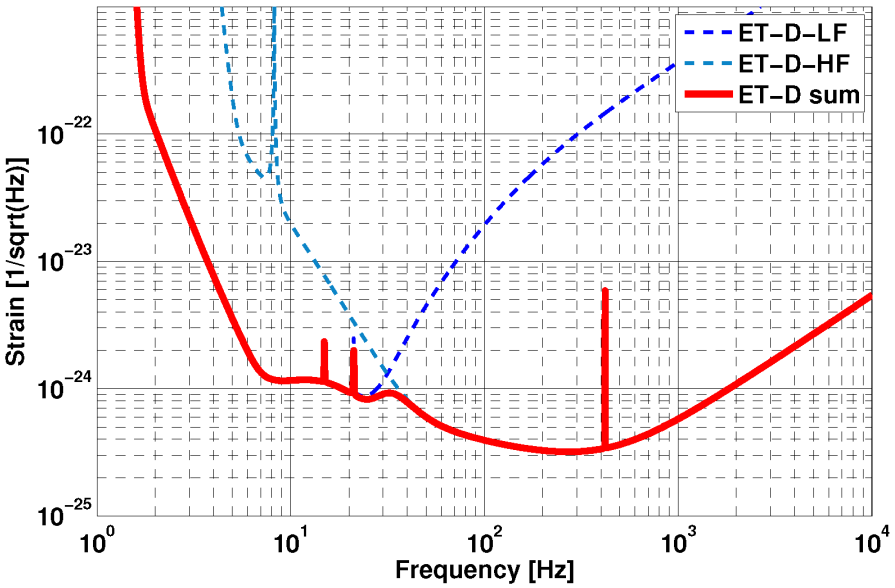

Figure 1.7: Planned sensitivity for a pair of interferometers of the Einstein Telescope xylophone configuration, as a sum of the low frequency and high frequency tuned detectors [22].

Upgrades implemented to advanced detectors (A+ LIGO and Advanced Virgo+) will improve the sensitivity and thus increase the observable volume of the Universe. The past and planned future sensitivities for LIGO, Virgo and KAGRA are represented in Figure 1.6.

Proposed third-generation gravitational wave detectors - the Einstein Telescope (ET) in Europe and the Cosmic Explorer (CE) in the United States - will lead to an immense increase in sensitivities. The projected sensitivities for ET and CE are shown in Figure 1.7 and Figure 1.8. The sensitivity of a detector is crucial in determining the distance to which it can observe an astrophysical source. By improving the sensitivity of third-generation detectors by a factor of approximately 10, the observable volume of the Universe could be increased by a factor of 1000. This would allow for the detection of previously unseen gravitational wave sources and also improve the detection signal-to-noise ratio (SNR) of specific emission mechanisms such as core-collapse supernovae, isolated neutron stars, black hole mergers at high redshifts, tidal effects at higher frequencies, and X-ray binaries.

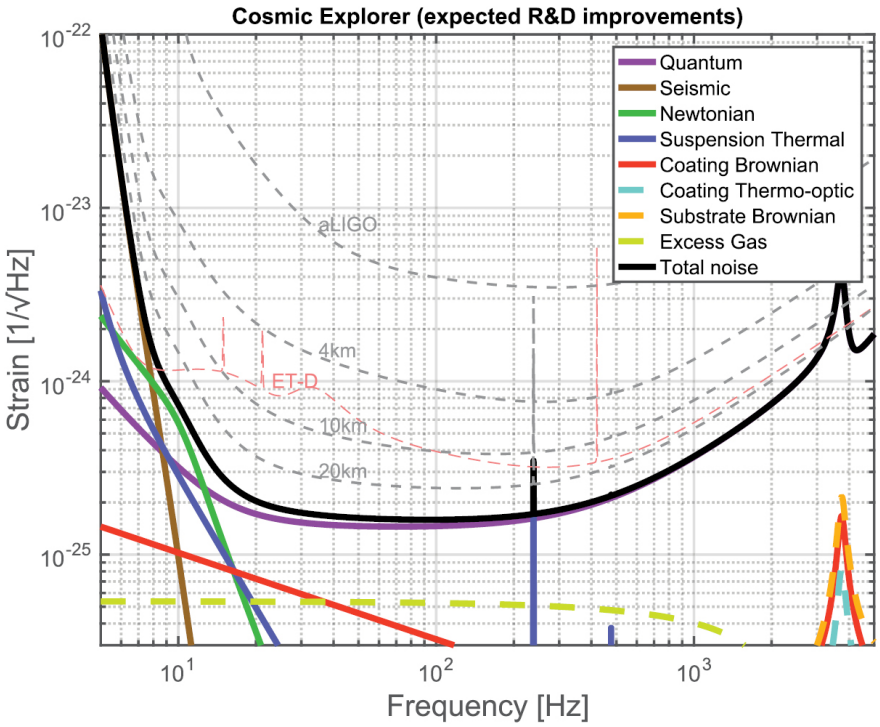

Figure 1.8: Planned sensitivity and expected noise budget of the Cosmic Explorer [23].

1.4 Sources of Gravitational Waves

We have seen that the emission of gravitational waves is associated with the second time derivative of the mass quadrupole moment of a system.The gravitational waves produced by everyday objects like humans and cars are too weak (the mass is too small) to be detected by any of the current detectors. So, we look towards the cosmos for cataclysmic events causing strong gravitational waves. Even for these massive events, the order of magnitude of the amplitude of the waves is very small [1].

The detectable gravitational waves are categorised into four different types:

- Compact binary inspiral gravitational waves: Compact binary systems include binary neutron star (BNS), binary black hole (BBH) and neutron star-black hole binary (NSBH). All the three types have the same characteristic waveform, also called as 'chirp'. A chirp is a signal in which the frequency increases (or decreases, but in this case it increases) with time (Figure 1.9). As the two compact objects spiral inward towards each other due to the emission of GWs, the corresponding waveform increases in frequency and amplitude. Followed by the

inspiral phase is the 'merger', where the two objects plunge toward each other and merge. After the merger, the system, which is now a black hole or a neutron star, settles down to its ground state after radiating away energy stored in its excited modes in the 'ringdown' phase (see Figure 1.10). Till date, all the GW signals that we have detected are compact binary mergers.

The matched filter technique is the conventional method for the detection and analysis of gravitational waves from compact binary coalescences. It was used for detecting GW150914 shown in Figures 1.9 and 1.10 [1]. It checks if the data contains any signal that matches with a template from the template bank that we have. These templates describe systems of merging binaries with varied masses, spins and the distance of the system from the Earth.

Consider the signal time series to be given by s and the template to be h. The optimal value of the matched filter SNR is given by

$$\left(\frac{S}{N}\right)^2 = 4\int_0^\infty \frac{|\tilde{h}(f)|^2}{S_n(f)}\,df \tag{1.12}$$

where $\frac{S}{N}$ is the signal-to-noise ratio, $\tilde{h}$ is the Fourier transform of h, and $S_n(f)$ is the one-sided noise power spectral density.

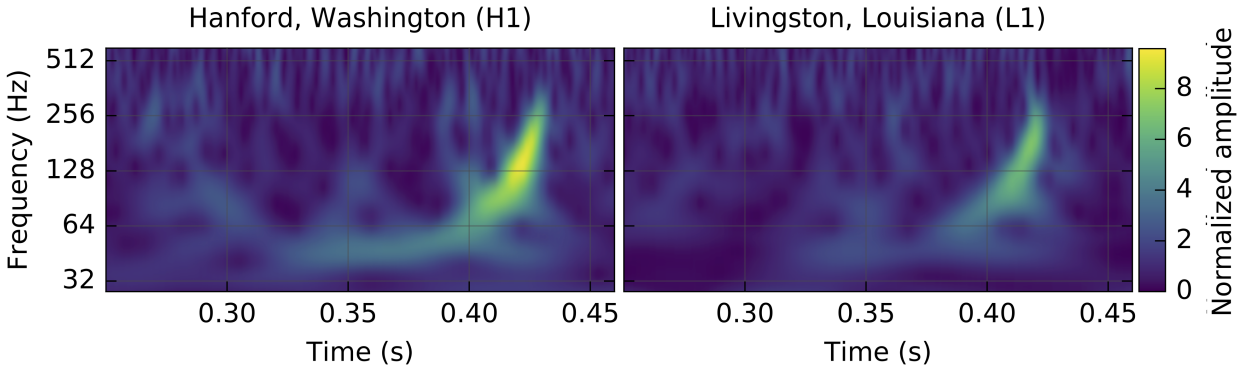

Figure 1.9: The two plots (LIGO Hanford on the left, LIGO Livingston on the right) show how the GW strain produced by the event GW150914 varied as a function of time and frequency. Both plots display he frequency sharply increasing, a characteristic of the chirp signal [1].

- Continuous gravitational waves: They are generated by objects like spinning neutron stars. As the star spins, any asymmetries in its spherical shape will produce gravitational waves.
- Stochastic gravitational waves: Also known as the gravitational wave background, the

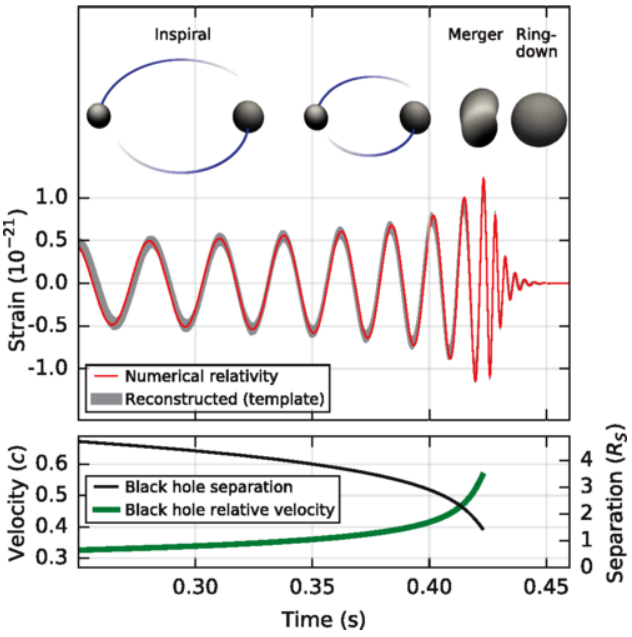

Figure 1.10: The top panel shows the numerical relativity models of the black hole horizons as the black holes of GW150914 merge (in red), and the reconstructed waveform of the event (in grey). It also displays the different phases of the event: inspiral, merger and ringdown. The bottom panel shows the Keplerian effective black hole separation and the effective velocity is shown as a function of time [1].

stochastic background is a statistically random signal from the early evolution of the Universe. This signal will be the same from every part of the sky (similar to CMB).

- Burst gravitational waves: They come from short-duration unknown or unanticipated sources. While it has been postulated that certain phenomena, such as supernovae and gamma-ray bursts, may generate these waves, the characteristics of the resulting signals cannot be accurately predicted due to an incomplete understanding of the underlying mechanisms.

Gravitational waves from core-collapse supernovae are an example of a burst signal. In this thesis, we are going to exclusively focus on signals from CCSNe.

1.4.1 Core-Collapse Supernovae

Supernovae can be classified into two broad types - Type I (H lines absent) and Type II (H lines present) on the basis of the presence of H lines at peak luminosity. It was realised that this

classification by itself is not enough and that each of these two types has further sub-types distinct from each other.

- Type Ia: Strong Si absorption lines in the spectrum taken near maximum luminosity
- Type Ib: Does not show Si absorption lines in the spectrum taken near maximum luminosity, but shows He lines
- Type Ic: Shows neither Si nor He lines

Type-Ia supernovae are typically thermonuclear explosions of white dwarfs, and type-II, type-Ib and type-Ic involve the collapse of stellar cores, which is what we are interested in.

A star with initial mass M spends $\sim 10^{10}\ (M/M_\odot)^{-2.5}$ years in the main sequence phase, where $M_\odot$ is the solar mass, slowly burning its hydrogen fuel into helium [24]. After the hydrogen fuel is exhausted, the next stages of nuclear burning produce heavier and more bound nuclei. The least massive stars eventually evolve into white dwarfs, where the electron degeneracy pressure is sufficient to halt the gravitational collapse of the star. These stars typically have an initial mass of $\lesssim 9\ M_\odot$.

Stars slightly more massive than these ($9\ M_\odot \lesssim M \lesssim 10\ M_\odot$) may produce supernovae. The degenerate electrons in the core get captured by Ne and Mg nuclei, thus triggering the collapse of the core. The core collapses to a proto-neutron star (PNS), and the stellar envelope is expelled by the shock produced at the bounce. If thermonuclear burning of oxygen is strong enough to overpower the collapse, the star may undergo a thermonuclear explosion with an iron-rich white dwarf left behind.

For stars with $9\ M_\odot \lesssim M \lesssim 100\ M_\odot$, nuclear burning proceeds till the formation of an iron core. At T $\sim 10^{10}$ K, iron nuclei dissociate into free nucleons and alpha particles. The core contracts further because of the absorption of thermal energy. Furthermore, the free protons and nucleons capture electrons, reducing the pressure even more. This triggers the dynamical collapse of the core.

In stars with $M \gtrsim 100\ M_\odot$, photons start producing e^+ and e^- pairs after carbon burning, converting thermal energy to rest mass. This triggers gravitational collapse by reducing the adiabatic index below 4/3. It continues till black hole formation for stars with $M \gtrsim 260\ M_\odot$. For stars with $100\ M_\odot \lesssim M \lesssim 200\ M_\odot$, if thermonuclear reactions are strong enough to overcome

gravitational collapse, pair-instability supernovae exploding with energies as high as $\sim 10^{53}$ erg might occur [5].

1.4.2 Explosion!

After the collapse of the core is triggered, it is on a free-fall timescale of ~0.3 s. During this process, the inner core collapses at a subsonic rate, while the outer core collapses supersonically. The collapse is abruptly halted upon reaching supranuclear densities, leading to the launch of a shock wave into the still-infalling outer core due to the bounce of the inner core. As the shock progresses outward, it loses energy due to the dissociation of iron nuclei, eventually forming a stalled accretion shock at ~150 km within ~10 ms after formation. To produce a supernova explosion and a stable neutron star remnant, the shock wave has to revive within a few hundred milliseconds and expel the infalling outer shells. Otherwise, the stellar matter keeps accumulating on top of the PNS, leading to the PNS being pushed beyond its stability limit and ultimately forming a black hole.

The revival of the shock wave is a topic of active research. Several mechanisms have been proposed [25]. We discuss some of them here.

Bounce-Shock Mechanism

The shock wave launched at the moment of core bounce causes the prompt ejection of the stellar matter. However, research indicates that this mechanism cannot lead to a successful explosion of any progenitor star. The inner core bounce is too weak to transfer enough energy to the shock wave [25].

Neutrino-Heating Mechanism

This mechanism is thought to occur in most core-collapse supernovae. As the PNS cools, it radiates neutrinos and antineutrinos of all three flavours (i.e. electron, muon and tau neutrinos and antineutrinos). They are absorbed by neutrons and protons, leading to neutrino heating. Of the $\sim 10^{53}$ erg of energy released by the PNS through the neutrinos, only ~1% is needed to be absorbed behind the shock to lead to the explosion [26] with energies $\sim 10^{50}$ erg. Hydrodynamical simulations show that violent convective and standing accretion shock instability (SASI) activity are important for the neutrino-heating mechanism to succeed. However, the nature of SASI and

the exact contribution of the hydrodynamic instabilities and turbulent motions for the onset of the explosion is a matter of active research [25].

Magnetohydrodynamic Mechanism

Also referred to as magnetorotational, this mechanism is a way to transfer energy from a highly magnetized neutron star to the outer layers. As the core of the PNS has very low resistivity, the magnetic field lines are frozen. The non-radial magnetic field and the related energy density increases due to magnetic flux conservation [25]. Magnetorotational instabilities, which require strong differential rotation between the PNS and the infalling matter, can increase the magnetic field [27]. This can lead to the expulsion of stellar matter in several ways. This mechanism is particularly important to drive the more energetic supernovae explosions.

Acoustic Mechanism

Based on sound waves produced in the inner core, a new CCSN mechanism was put forth [28]. After bounce ($\gtrsim$1 s), large amplitude gravity-mode oscillations of the PNS core are excited by SASI and through anisotropic accretion. This gravitational energy due to accretion is converted into sound through core oscillations. The PNS vibrations (with amplitudes of several km) are dampened by the strong sound waves propagating into the surrounding medium. As the waves reach regions with lower densities away from the PNS they evolve into secondary shocks, effectively heating the post-shock region and leading to the explosion. This mechanism is currently not as popular in the scientific literature as the neutrino-heating mechanism.

Chapter 2

Data and Methods

Gravitational waves from core-collapse supernovae are relatively uncommon occurrences that are difficult to detect. The aLIGO-Virgo network has been shown to have a limited sensitivity range for detecting these types of events [29], and can currently observe them only within a few kiloparsecs (kpc) from Earth. Moreover, the estimated rate of core-collapse supernovae in galaxies similar in size to the Milky Way is only once or twice per century [30], making detection even more challenging. To compound the issue, an unmodelled search approach is required, further reducing the detection probability of gravitational waves from these events. This study focuses specifically on core-collapse supernovae and utilizes an unmodelled search pipeline in an effort to detect these elusive events.

2.1 Datasets

As discussed in Section 1.2.2, terrestrial detectors are sensitive to GWs as well as different noise sources. The Einstein Telescope is no exception. Figure 2.1 shows the estimated sensitivity curve of the Einstein Telescope. We first produced a time series following the Gaussian distribution. It was subsequently recoloured using the power spectral density of the Einstein Telescope. Thus, we now have a time series comprised entirely of noise, absent of any GW signals.

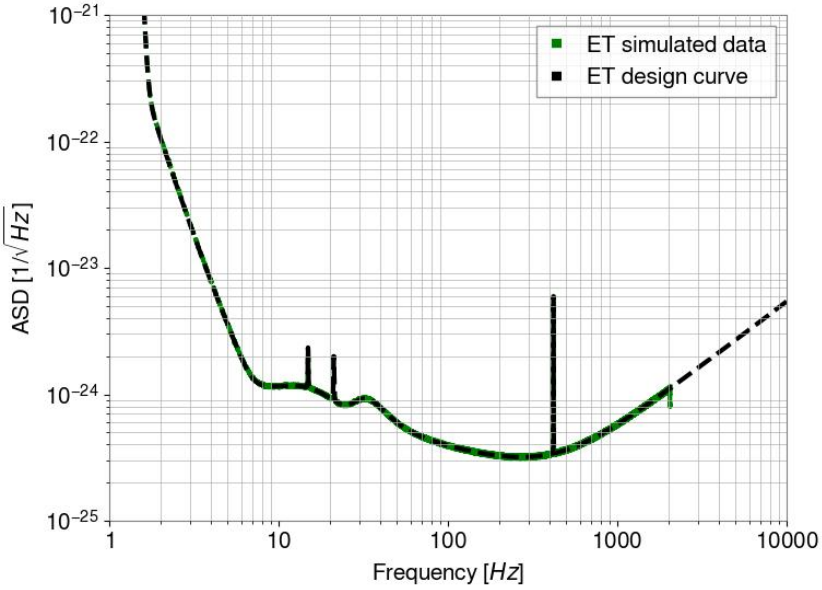

Figure 2.1: Noise sensitivity curve of the Einstein Telescope which was used to generate the noise time series.

Supernova Waveforms

We used waveforms obtained through three-dimensional simulations, such as those detailed in [31]. The waveforms are generated according to the different explosion mechanisms. Each physical mechanism produces a different waveform. We want to study the properties of core-collapse supernova and understand the underlying mechanism, so utilising different types of waveforms is crucial. We consider waveforms simulated using the neutrino explosion and magnetorotational explosion mechanisms, as discussed in Section 1.3.2. We also include the case of no explosion, i.e., the stalled shockwave fails to get re-energised, and the core collapses onto itself, resulting in a black hole. Chirplets have also been included in the set of waveforms. These waveforms are displayed in Figure 2.2.

Model s18np

It is a non-rotating, solar metallicity progenitor star (massive red supergiant progenitor) with a zero-age main sequence (ZAMS) mass 18 $M_\odot$ from [32] simulated with the stellar evolution code KEPLER. The simulation ends at 0.56 s after core bounce, at which time the GW emission has decreased substantially. The peak GW amplitude is $\sim$ 5 cm at the source. This model fails to explode without the strong convective seed perturbations present in model s18. In the current

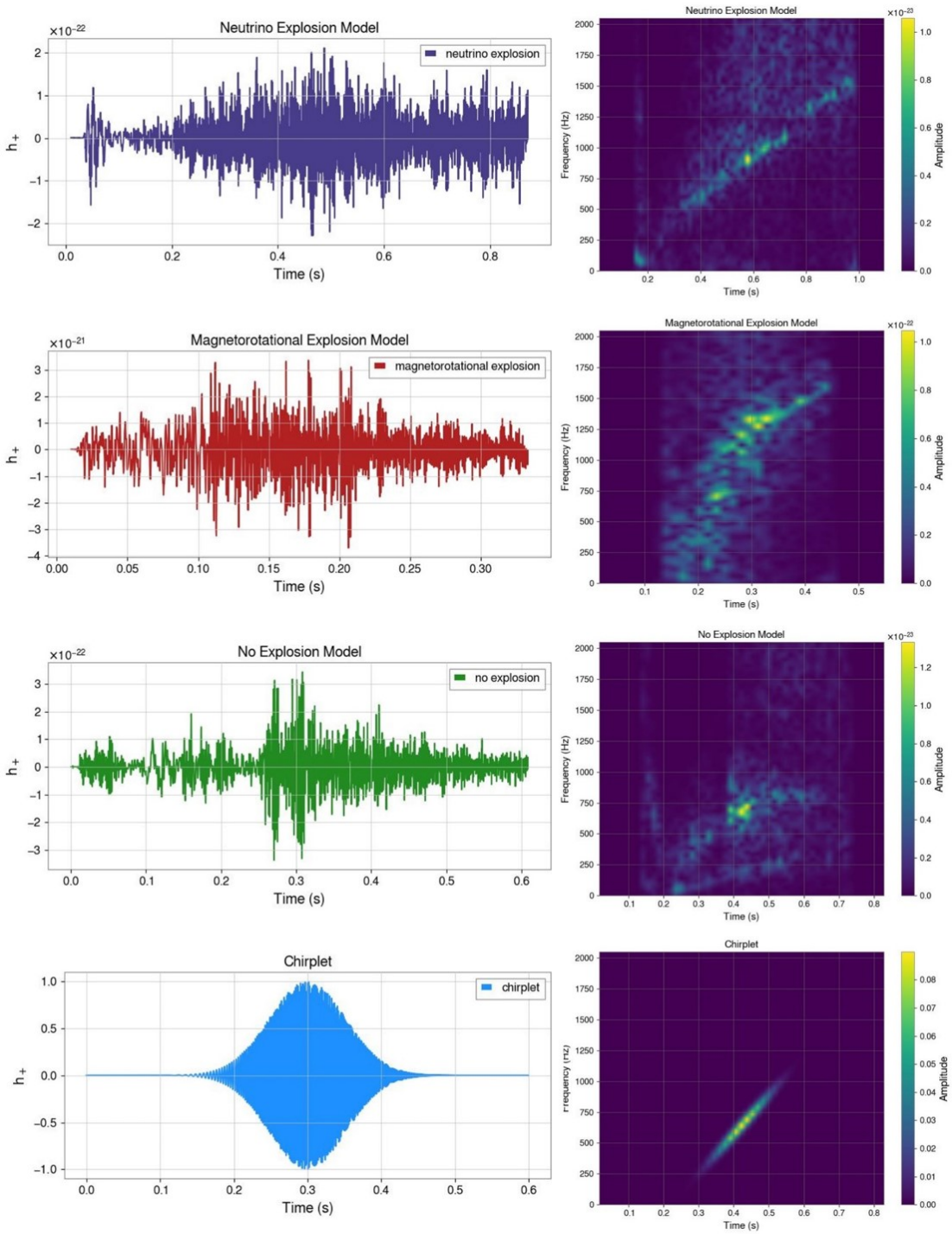

Figure 2.2: The GW signals for the mechanisms used in this analysis. Top to bottom: Neutrino explosion, magnetorotational explosion, no explosion and chirplet. The left column shows the time series and the right column shows the time-frequency representation of the signals.

detectors, this model is only detectable within our Galaxy. With the Einstein Telescope, s18np can be detected up to a few hundred kpc.

Model C15

It is a non-rotating progenitor star with a ZAMS mass of 15 $M_\odot$ from [33] simulated with the neutrino hydrodynamics code CHIMERA. The peak GW amplitude is $\sim$ 6 cm at the source. This model fails to explode.

Model s18

It is a solar metallicity progenitor star with a ZAMS mass of 18 $M_\odot$ from [31] simulated using the neutrino hydrodynamics code COCONUT-FMT. The simulation ends at 0.89 s after core bounce. This model produces a neutrino-driven explosion $\sim$ 250 ms after the bounce. The peak GW amplitude is $\sim$ 10 cm at the source and the GW frequency peaks between 800 and 1000 Hz. An explosion such as model s18 will be detectable to about 17.5 kpc by the LIGO and Virgo detectors and to about 180 kpc with the ET.

Model s12

It is a non-rotating, solar metallicity progenitor star with a ZAMS mass of 15 $M_\odot$ from [34] simulated using the radiation/hydrodynamic code FORNAX. The simulation in 1D ends 10 ms after core bounce, and fluid and neutrino-radiation quantities are then remapped to 3D. This model produces a neutrino-driven explosion.

Model m39

It is a rapidly rotating, low metallicity progenitor star (rapidly rotating Wolf-Rayet star) with an initial helium star mass of 39 $M_\odot$ from [32] simulated with the Modules for Experiments in Stellar Astrophysics (MESA) stellar evolution code. The simulation ends at 0.98 s after core bounce. This model produces a neutrino-driven explosion a few hundred milliseconds after core bounce, leaving behind a neutron star as a remnant. Model m39 reaches a few hundred kpc with current detectors, beyond the Large Magellanic Cloud at 50 kpc. With the ET, it is detectable up to almost 2 Mpc (i.e. through the Local Group).

Model m39_B12

It is a rapidly rotating, low metallicity progenitor star with a ZAMS mass of 39 $M_\odot$ from [35] simulated using the stellar evolution code MESA. The simulation ends 0.68 s after core bounce. This model produces a magnetorotational explosion. The peak GW amplitude is $\sim$ 165 cm at the

source, and the GW frequency peaks at ~ 2000 Hz. The GW emission will be detectable out to distances of ~ 4 Mpc in the Cosmic Explorer detector and up to ~ 2 Mpc in the Einstein Telescope detector.

Model a13

It is a rapidly rotating, subsolar metallicity progenitor star (Wolf-Rayet star) with a ZAMS mass of 13 $M_\odot$ from [36] simulated using the stellar evolution code MESA. This model produces a magnetorotational explosion leaving behind a black hole as a remnant.

Chirplet

It can be considered to be a burst signal with a similar duration to a CCSN signal and similar characteristics to one in the time-frequency domain. It has been added to compare the case where a similar signal which is not a CCSN is detected.

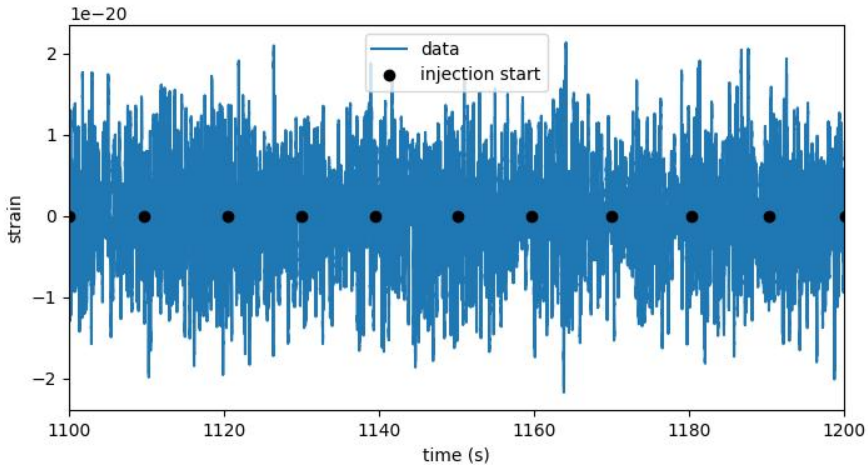

Figure 2.3: The data used in this analysis: the final time series (blue) and injections (black)

We injected the waveforms from these models into the recoloured noise time series. We have 46 injections per model, and 45 chirplets were injected. The total number of injections is 367. Of these, 92 signals were from the non-exploding models, 138 from the neutrino-driven explosion models, 92 from the magnetorotational explosion models, and 45 were chirplets. To ensure that each signal was well-separated from the other and that there was no overlap between them, each waveform was added at regular intervals of 10 seconds. This ensured that each signal was distinct and allowed for accurate analysis, given that typical signals are only approximately one second long. The resulting data is shown in Figure 2.3.

2.2 Detection Pipeline

In the case of gravitational waves from core-collapse supernovae, the matched filter cannot be used. The dynamics of the explosion of the core are not completely understood. The processes involved are largely stochastic, such as turbulent connection between the proto-neutron star and the shock front [37]. This stochasticity gets added to the gravitational waves emitted by the explosion, and it is, therefore, difficult to model them. So we cannot use the matched filter technique to analyse the gravitational waves from core-collapse supernovae. Methods agnostic to the signal waveform must be used.

Wavelet Detection Filter

The Wavelet Detection Filter is a wavelet-based event trigger generator. It does not require a well-defined waveform for detecting a signal. WDF decomposes the data into multiple time-frequency resolution maps based on the wavelet transform [38]. A time series $s(t)$ can be projected onto a family of mutually orthonormal wavelets using WDF as follows:

$$\langle s|\psi_{a,b}\rangle = \int_{-\infty}^{\infty} s(t)\frac{1}{\sqrt{b}}\psi^*\left(\frac{t-a}{b}\right)\,dt$$

where ψ^* is the complex conjugate of the mother wavelet, parameter b sets the scale of the time-frequency map, and a is the time-shifting parameter. WDF utilises a bank of wavelets such as the Daubechies, Haar and spline wavelets for the analysis of transients. [38]

WDF takes in various parameters to analyse the data. Some of these are:

- window: the analysing window for WDF (in units of data values); here, window = 1024
- overlap: the overlap (in units of data values) between two consecutive windows for WDF analysis; here, overlap = 896
- threshold: the minimum value of WDF signal-to-noise ratio to identify a trigger; here, threshold = 0.2
- len: the time window (in seconds of data) loaded in the loop

- ARorder: the order of Auto-Regressive (AR) model for whitening; here, ARorder = 2000
- learn: the length (in seconds) of the data used to estimate AR parameters; here, learn = 200

It calculates the wavelet coefficients, and the inverse wavelet transform parameters, which are later used in the reconstruction process.

2.3 Whitening

The detectors produce non-stationary output, which poses a challenge for detection algorithms designed for stationary Gaussian white noise. Gaussian white noise possesses the property of statistical independence between any two values at different time instances. To combat stationary noise and render the noise background more uniform, a technique called whitening is employed. Whitening aims to reduce the impact of noise frequencies and equalize their likelihood of occurrence. As a result, the auto-correlation of the signal is narrowed and approaches a delta function. This results in a uniform background across all frequencies, with any signals appearing as anomalous spikes in this background (Figure 2.4).

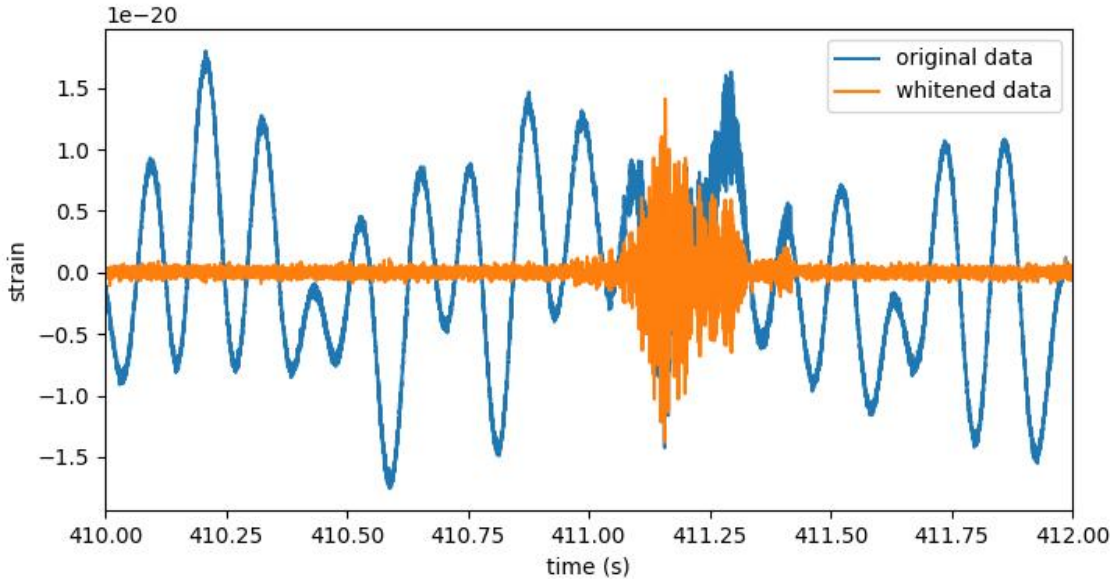

Figure 2.4: The time series of the data before and after whitening.

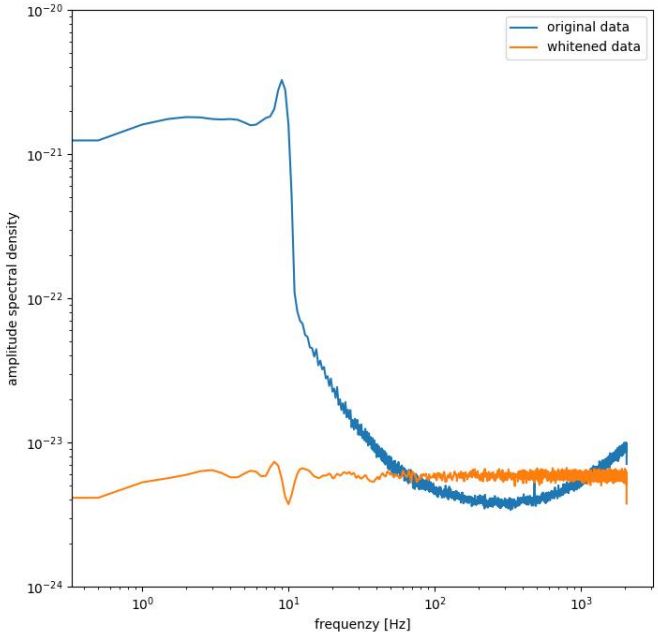

Figure 2.5: The amplitude spectral density of the data before and after whitening.

The whitening procedure carried out by WDF builds a parametric model of the stationary noise PSD in order to suppress it by applying weighting factors to the data. This corresponds to the application of a time-domain filter to the data. The noise PSD is fitted using an autoregressive (AR) model of order 2000, and the AR parameters are computed using the first 200 seconds of each dataset [39]. To speed up this step, the data is divided into smaller parts and allocated to different central processing units (CPUs) for parallel processing.

The PSD of a white process is constant, i.e., the power per unit frequency remains the same over the entire frequency range. In Figure 2.5, we show an example of the PSDs, computed with the Welch method as described in [40], before and after the whitening procedure is carried out by WDF. The whitened data has a flat PSD profile, meaning that the stationary contribution of noise has been successfully mitigated.

2.3.1 Wavelet Denoising

Following the whitening process, the wavelet coefficients are expected to contain characteristics of the transient waveforms on different frequency and time scales. Specifically, the Donoho and Johnstone method [41] is employed to select only the relevant coefficients, which sets a lower threshold t on the absolute value of the wavelet coefficients $|w_i|$ as

$$t = \sqrt{2 \log N} \hat{\sigma} \tag{2.1}$$

where N is the number of window data points and $\hat{\sigma}$ is the estimation of the noise standard deviation [38].

The WDF window size used in this analysis is 1024 points with an overlap of 896 between consecutive windows. In time, the two correspond to 0.5 s and 0.4375 s, respectively, for a sampling frequency of 2048 Hz. The data has been downsampled to 2048 Hz from an original frequency of 4096 Hz.

2.4 Trigger Generation

Wavelet Detection Filter (WDF) operates on data in segments, where each segment is defined by a window of a specific size. Within each window, WDF calculates wavelet coefficients and assesses the signal-to-noise ratio (SNR_w) against a pre-set threshold. The SNR_w is given by

$$SNR_w = \frac{\sqrt{\frac{\sum_{i=1}^{N} r_i^2}{N}}}{\hat{\sigma}} \tag{2.2}$$

where r_i stands for the reconstructed signal and N stands for the number of window data points.

If the SNR exceeds the threshold, WDF generates a trigger, which records important information about the data segment, such as the start time, peak SNR time, minimum, maximum, and mean frequencies, duration of the event, and wavelet coefficients.

2.5 Clustering

Core-collapse supernovae signals are typically of one-second duration, which is longer than the WDF window size used for analysis in this study. Consequently, the analysis process may generate multiple closely spaced triggers for a single CCSN signal (see Figure 2.6). However, for an optimal signal representation, it is desirable to have only one trigger corresponding to each signal. To achieve this objective, a clustering process is employed, wherein the triggers are grouped based on their proximity in time, frequency, and SNR so that only one representative trigger is selected for each signal.

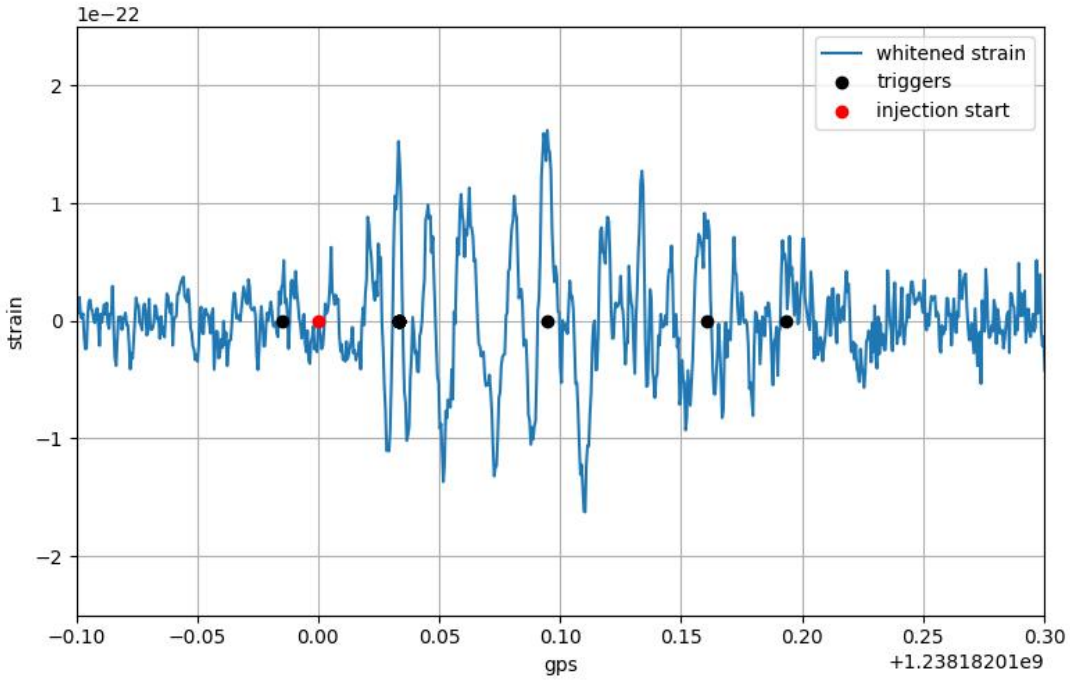

Figure 2.6: An injected signal (in red) with multiple triggers (in black); the blue time series is the whitened data.

Various criteria can be applied for the clustering of triggers. One of the most straightforward and elementary approaches is to cluster those triggers that are closer to each other in time (time at the peak of the trigger SNR), specifically in terms of their peak GPS. To further refine the clustering process, additional factors may be incorporated. For instance, the inclusion of both time and frequency enables the grouping of triggers that are nearer to each other in both dimensions,

using mean frequency as the criterion. To establish more stringent clustering conditions, the SNR can be included too. This involves using time, mean frequency, and WDF energy to group together triggers.

After grouping the triggers together, the trigger parameters are updated for the group as follows:

- gpsStart: the least value of gpsStart in the group of triggers
- gpsPeak: the gpsPeak of the trigger with the highest snrPeak
- EnWDF: the average of EnWDF of all the triggers
- snrMean: the average of snrMean of all the triggers
- snrPeak: the highest snrPeak in the group of triggers
- freqMean: the average of freqMean of all the triggers
- freqPeak: the freqPeak of the trigger with the highest snrPeak
- freqMin: the least freqMin in the group of triggers
- freqMax: the highest freqMax in the group of triggers
- wave: the wave of the trigger with the highest snrPeak

This is how a 'clustered trigger' is produced. Thus, instead of having multiple triggers, there remains only one trigger with the parameters defined as above.

2.6 Reconstruction

Signal reconstruction plays a crucial role in the analysis of gravitational waves, particularly in parameter estimation, where accurate waveform reconstruction is essential. In the case of compact binary coalescence (CBC) signals, the use of pre-existing template banks and matched filtering enables easy reconstruction and subsequent parameter estimation. However, for core-collapse supernovae signals, which lack a fixed template, the ability to reconstruct waveforms from diverse

explosion mechanisms becomes even more critical. Thus, developing effective methods for the waveform reconstruction of CCSNe signals is important for accurate parameter estimation.

In the process of analysing gravitational wave data, we transformed it from the time domain to the wavelet domain using WDF. Following this transformation, reconstruction entails a reversal of this process. We do an inverse wavelet transform that returns the data to the time domain.

Along with the wavelet coefficients, WDF also allows for the computation and storage of the reconstructed signal time series (given by rw's, the inverse wavelet transform coefficients) of the selected analysis window in the trigger files. This corresponds to the time series obtained by carrying out the inverse wavelet transform.

As discussed previously, a signal can be longer than the WDF window used. Thus, there might be multiple triggers corresponding to that same signal. Each of these triggers will have a set of reconstructed time series (rw's) associated with it. Hence, the final reconstruction must take into account the overlapping windows and the rw's in the overlapping stretches of data must be averaged. This ensures that the reconstruction is smooth and continuous.

It is to be noted that the wavelet denoising procedure involves some extent of data compression. Wavelet coefficients lower than the threshold are set to zero. It is possible that these coefficients may carry some information about the signal. Therefore, some information is lost while doing inverse wavelet transform in the computation of the rw's.

Chapter 3

Results and Discussion

In this chapter, we present the findings obtained from the clustering and reconstruction of gravitational wave signals from core-collapse supernovae. The first section of this chapter discusses the clustering of triggers based on different conditions, including time, frequency, and signal-to-noise ratio. The second section presents the results of the reconstruction process and evaluates the accuracy of the reconstructed signal. The analysis also includes the detection rate and accuracy for different explosion mechanisms, such as neutrino explosion, magnetorotational explosion, and chirplets.

3.1 Clustering

We generated triggers using WDF. Table 3.1 shows an example of the data contained in the list of triggers. As discussed in Section 2.5, we clustered triggers using all three cases - time, time and frequency, and time, frequency and SNR. The results of all the cases are shown in Figure 3.2. A slice of the dataframe with clustered triggers is shown in Table 3.2. It can be seen that several triggers from Table 3.1 have been merged into one in Table 3.2.

The clustering process works as expected (Figure 3.1). For the example shown in Figure 3.1, the clustering process was able to merge about nine triggers into one. As expected, the peak GPS of the clustered trigger shows up right where the signal in the bottom plot peaks.

gpsStart	gpsPeak	EnWDF	snrMean	snrPeak	freqMin	freqMean	freqMax	freqPeak
1238179842.750	1238179843.014	0.916	0.577	2.226	10.000	78.923	186.000	92.000
1238179842.812	1238179843.014	0.774	0.532	2.198	16.000	81.500	186.000	64.000
1238179842.875	1238179843.014	0.785	0.535	2.145	10.000	79.731	186.000	74.000
1238179842.938	1238179843.014	0.809	0.552	2.112	10.000	80.308	182.000	74.000
1238179843.000	1238179843.014	0.768	0.556	2.049	8.000	78.500	182.000	26.000

Table 3.1: An example of the trigger dataframe (only a few rows and columns are shown)

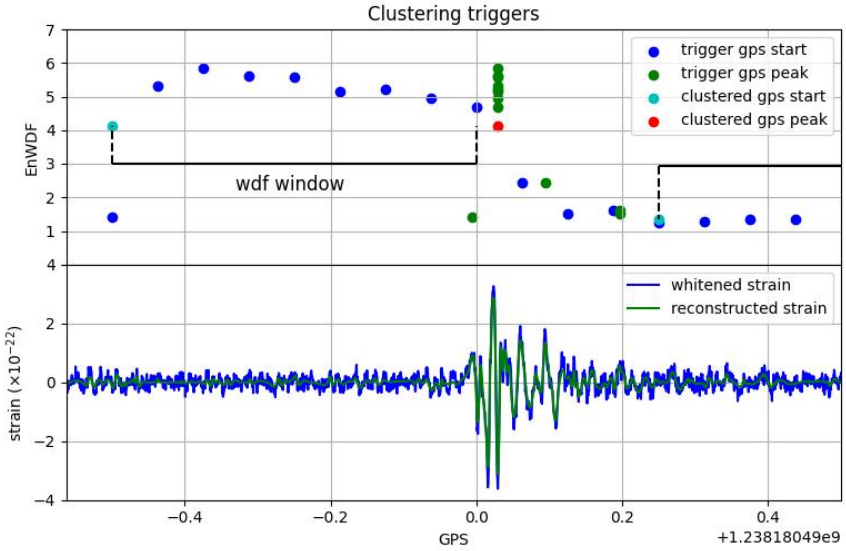

Figure 3.1: An example of a clustered trigger. The top panel shows the triggers detected and clustered, the bottom panel shows the segment of whitened strain and reconstructed strain.

The clustering of triggers works best when only the time condition is used. The process is able to merge all the triggers into one trigger, right at the peak of the signal. As further conditions are added to the clustering criteria, the results become poorer. The clustering in time and frequency is able to merge a few triggers, but not all. And on the other hand, in the case where time, frequency and SNR are all included, barely any of the triggers get clustered. It shows the poorest results in all three cases that we considered.

gpsStart	gpsPeak	EnWDF	snrMean	snrPeak	freqMean	freqPeak	freqMin	freqMax
1238179842.750	1238179843.014	0.810	0.551	2.226	79.792	92.000	8.000	186.000
1238179843.062	1238179843.362	0.727	0.505	1.461	69.731	40.000	8.000	174.000
1238179843.375	1238179844.015	0.860	0.597	3.365	73.027	68.000	8.000	206.000
1238179844.188	1238179844.343	0.559	0.365	1.365	75.788	38.000	10.000	188.000
1238179844.438	1238179845.171	0.571	0.383	1.552	74.561	66.000	8.000	192.000

Table 3.2: An example of the clustered trigger dataframe

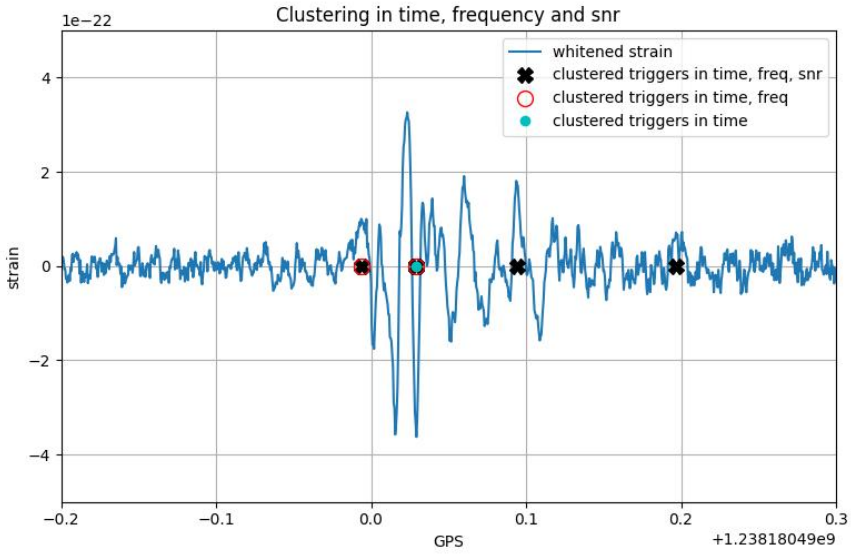

Figure 3.2: Clustering using three different cases: [i] time; [ii] time and frequency; [iii] time, frequency and SNR

The choices of the clustering parameters were made on the basis of the characteristics of the CCSNe signals. The length of a typical CCSNe signal is of the order of a second. The time parameter was chosen accordingly. As such, these parameters can be customised for different types of gravitational wave signals.

3.2 Reconstruction

Reconstruction is an important step for parameter estimation. We were able to reconstruct the signal to a fairly good accuracy (see Figure 3.3). The reconstructed strain follows the whitened strain quite closely. The residual error between the two is displayed in Figure 3.4. As can be seen in the plot shown in Figure 3.4, the error in reconstruction is minimal.

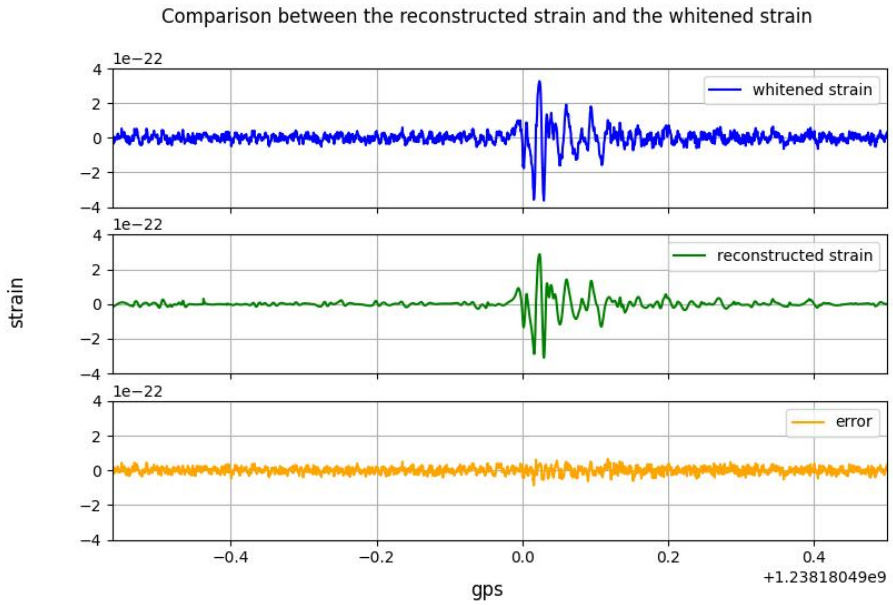

Figure 3.4: The error in reconstruction as compared with the whitened strain. Here, the error is the residual between the reconstructed strain and the whitened strain.

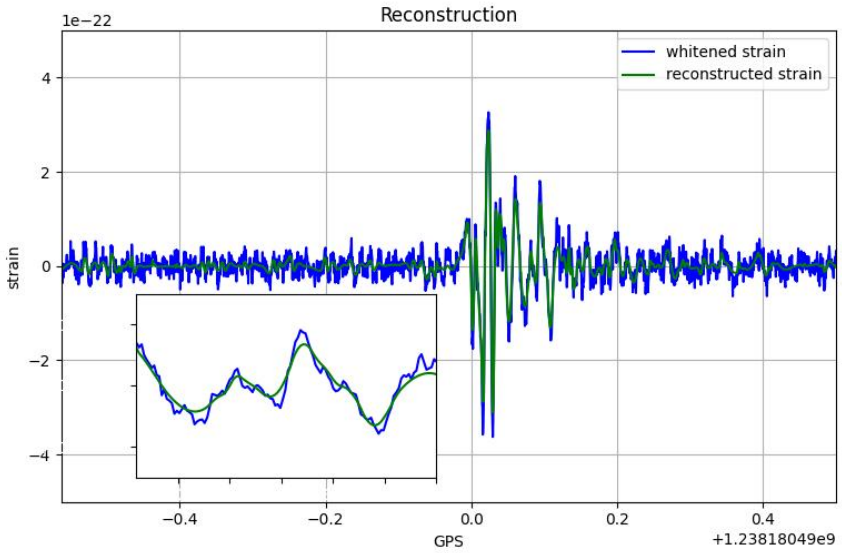

Figure 3.3: An example of signal reconstruction. The reconstructed strain (in green) closely follows the whitened strain (in blue).

We measured the accuracy of reconstruction using the mean absolute error (MAE) and the mean squared error (MSE) for the signals belonging to all the mechanisms. These metrics were

Explosion Mechanism	Mean Absolute Error	Mean Squared Error	Total number of signals in the injected data
No Explosion	1.43734523431573E-23	4.75132527147505E-46	92
Neutrino Explosion	1.45406097181378E-23	3.92656088658942E-46	124
Magnetorotational Explosion	1.37131718013514E-23	3.12871694815247E-46	85
Chirplet	1.24594152431531E-23	2.50386110026416E-46	21

Table 3.3: Errors in reconstruction calculated for all the mechanisms.

calculated according to the following formulae:

$$\text{MAE} = \frac{\sum_{i=1}^{n} |h_i - r_i|}{n}, \quad \text{MSE} = \frac{\sum_{i=1}^{n} (h_w - r_i)^2}{n} \tag{3.1}$$

where h_i is the whitened time series, r_i is the total reconstructed time series, and n is the number of triggers considered for the analysis of a particular signal. The values thus obtained were averaged for signals belonging to the same explosion mechanisms.

- No explosion: $\text{MAE} = 1.43735 \times 10^{-23}, \quad \text{MSE} = 4.75133 \times 10^{-46}$
- Neutrino explosion: $\text{MAE} = 1.45406 \times 10^{-23}, \quad \text{MSE} = 3.92656 \times 10^{-46}$
- Magnetorotational explosion: $\text{MAE} = 1.37132 \times 10^{-23}, \quad \text{MSE} = 3.12872 \times 10^{-46}$
- Chirplet: $\text{MAE} = 1.24594 \times 10^{-23}, \quad \text{MSE} = 2.50386 \times 10^{-46}$

These values, along with how many signals were detected per mechanism, have been tabulated in Table 3.3. For the neutrino explosion mechanism, 124 signals out of the 138 total injected signals

Model	Mean Absolute Error	Mean Squared Error	Explosion Mechanism	Detected Signals (in percentage)
s18np	1.43629253723836E-23	4.59433413816736E-46	No explosion	100
c15	1.43839793139311E-23	4.90831640478272E-46	No Explosion	100
s18	1.39282735163588E-23	3.18183707741147E-46	Neutrino Explosion	80.43
m39	1.53411094063432E-23	5.04938005130461E-46	Neutrino Explosion	100
s12	1.41950842012690E-23	3.33888038324029E-46	Neutrino Explosion	89.13
m39_B12	1.29595970805320E-23	2.71720535022915E-46	Magnetorotational	86.96
a13	1.43830159976352E-23	3.49450503519541E-46	Magnetorotational	97.83
-	1.24594152431531E-23	2.50386110026416E-46	Chirplet	46.67

Table 3.4: Errors in reconstruction calculated for all the models.

were detected. For the non-exploding case, the entire 92 injected signals were successfully detected. For the magnetorotational explosion mechanism, 85 signals out of the total 92 injected signals were detected. And in the case of chirplets, we were able to detect 21 out of the 45 injected ones. The analysis was able to detect all the signals for the non-exploding case. On the other hand, the error in reconstruction is the least for chirplets, but the number of signals detected is the least in this case.

Table 3.4 displays MAE and MSE for all the models considered in this analysis. All the signals belonging to the s18, c15 and m39 models are detected, whereas only 21 out of the 45 injected signals representing chirplets were detected.

Chapter 4

Conclusions and Outlook

The detection of gravitational waves from core-collapse supernovae events remains a challenging task due to the low frequency of occurrence and the low sensitivity of current ground-based interferometers. However, an unmodelled search approach can provide a promising solution to detecting these elusive signals. In this study, we tested the capabilities of the Wavelet Detection Filter, an agnostic search pipeline, for detecting CCSNe signals using a third-generation interferometer, the Einstein Telescope (ET), which is expected to have greater sensitivity than Advanced LIGO and Advanced Virgo.

Our analysis focused on using 3D waveforms of signals as candidate CCSNe events, and we demonstrated that detection is possible in the direction of the Large Magellanic Cloud, for signals modelled initially at a distance of 10 kpc from Earth. We were able to detect signals with different explosion mechanisms, such as the neutrino-heating mechanism and the magnetorotational mechanism, and a range of injected SNRs (from 10 to 30). We then devised a clustering algorithm to group the triggers generated through the WDF. We performed the reconstruction process, averaging over the reconstructed time series to obtain the final total reconstructed signal for most of the injected signals. Our accuracy testing involved comparing the reconstructed data with the original whitened data using several metrics, and we found that the reconstruction process was generally effective. The next step in this study would be to characterise the reconstructed signals according to the explosion mechanisms. This would be done with machine learning techniques, particularly convolutional neural networks.

Although we focused solely on the ET detector in this work, a similar analysis is being carried

out for Advanced LIGO separately. We hope that our study will provide a perspective on the future gravitational wave studies from CCSNe, particularly in the area of signal reconstruction. Our findings can be useful for future parameter estimation studies and may contribute to the development of more advanced search techniques that can aid in the detection of gravitational waves from CCSNe.

In summary, the detection of gravitational waves from CCSNe is a challenging but important area of research that requires innovative search methods and advanced interferometers. Our study has shown that the WDF approach is a promising method for detecting CCSNe signals using the ET detector. The successful reconstruction of the signals we detected opens up opportunities for future studies in parameter estimation and other related areas. Overall, we believe that our work contributes to the growing body of knowledge on gravitational wave studies from CCSNe and will inspire further research in this field.

Bibliography

[1] B. P. Abbott et al. (LIGO Scientific Collaboration and Virgo Collaboration), *Observation of Gravitational Waves from a Binary Black Hole Merger*, Physical Review Letters 116, p. 061102, (2016).

[2] B. P. Abbott et al. (LIGO Scientific Collaboration and Virgo Collaboration), *GWTC-1: A Gravitational-Wave Transient Catalog of Compact Binary Mergers Observed by LIGO and Virgo during the First and Second Observing Runs*, Physical Review X 9, p. 031040, (2019).

[3] R. Abbott et al. (LIGO Scientific Collaboration and Virgo Collaboration), *GWTC-2: Compact Binary Coalescences Observed by LIGO and Virgo during the First Half of the Third Observing Run*, Physical Review X 11, p. 021053, (2021).

[4] The LIGO Scientific Collaboration and the Virgo Collaboration and the KAGRA Collaboration et al., *GWTC-3: Compact Binary Coalescences Observed by LIGO and Virgo During the Second Part of the Third Observing Run*, (2021).

[5] Ernazar Abdikamalov, Giulia Pagliaroli, and David Radice, *Gravitational Waves from Core-Collapse Supernovae*, (2020).

[6] Michele Maggiore et al., *Science case for the Einstein telescope*, Journal of Cosmology and Astroparticle Physics 2020, pp. 050–050, (2020).

[7] Christina Sormani, *A Two-Part Feature: The Mathematics of Gravitational Waves*, Notices of the American Mathematical Society 64, pp. 684–685, (2017).

[8] Sean M. Carroll, *Spacetime and geometry. An introduction to general relativity*, Provided by the SAO/NASA Astrophysics Data System, pp. 300–307, (2004).

[9] Robert H. Shumway and David S. Stoffer, *Time Series Analysis and Its Applications*, Springer New York, (2000).

[10] M. Maggiore, *Gravitational Waves: Volume 1: Theory and Experiments*, Gravitational Waves, OUP Oxford, (2008).

[11] M.G. Beker et al., *Seismic Attenuation Technology for the Advanced Virgo Gravitational Wave Detector*, Physics Procedia 37, pp. 1389–1397, (2012).

[12] Craig Cahillane and Georgia Mansell, *Review of the Advanced LIGO Gravitational Wave Observatories Leading to Observing Run Four*, Galaxies 10.1, (2022).

[13] F Acernese et al., *Advanced Virgo: a second-generation interferometric gravitational wave detector*, Classical and Quantum Gravity 32, p. 024001, (2015).

[14] Carlton M. Caves, *Quantum-Mechanical Radiation-Pressure Fluctuations in an Interferometer*, Physical Review Letters 45, pp. 75–79, (1980).

[15] F. Acernese et al. (Virgo Collaboration), *Increasing the Astrophysical Reach of the Advanced Virgo Detector via the Application of Squeezed Vacuum States of Light*, Physical Review Letters 123, p. 231108, (2019).

[16] B. P. Abbott et al. (LIGO Scientific Collaboration and Virgo Collaboration), *GW170817: Observation of Gravitational Waves from a Binary Neutron Star Inspiral*, Physical Review Letters 119, p. 161101, (2017).

[17] GravitySpy, *Gravity Spy*, URL: https://www.zooniverse.org/projects/zooniverse/gravity-spy.

[18] *GWitchHunters*, URL: https://www.reinforceeu.eu/demonstrators/gwitchhunters.

[19] B.P. Abbott et al. (LIGO-Virgo-KAGRA Collaboration), *Prospects for observing and localizing gravitational-wave transients with Advanced LIGO, Advanced Virgo and KAGRA*, Living Reviews in Relativity 23, p. 3, (2020).

[20] R. Abbott et al. (The LIGO Scientific Collaboration, the Virgo Collaboration), *Open data from the first and second observing runs of Advanced LIGO and Advanced Virgo*, SoftwareX 13, p. 100658, (2021).

[21] *LIGO/Virgo O3 Public Alerts*, (2020), URL: https://gracedb.ligo.org/superevents/public/O3/.

[22] S Hild et al., *Sensitivity studies for third-generation gravitational wave observatories*, Classical and Quantum Gravity 28, p. 094013, (2011).

[23] B P Abbott et al., *Exploring the sensitivity of next generation gravitational wave detectors*, Classical and Quantum Gravity 34, p. 044001, (2017).

[24] Stuart L. Shapiro and Saul A. Teukolsky, *Black holes, white dwarfs, and neutron stars : the physics of compact objects*, Provided by the SAO/NASA Astrophysics Data System, (1983).

[25] Hans-Thomas Janka, *Explosion Mechanisms of Core-Collapse Supernovae*, Annual Review of Nuclear and Particle Science 62.1, pp. 407–451, (2012).

[26] Anthony Mezzacappa and O.E.B. Messer, *Neutrino transport in core collapse supernovae*, Journal of Computational and Applied Mathematics 109.1, pp. 281–319, (1999).

[27] Shizuka Akiyama, J. Craig Wheeler, David L. Meier, and Itamar Lichtenstadt, *The Magnetorotational Instability in Core-Collapse Supernova Explosions*, The Astrophysical Journal 584, pp. 954–970, (2003).

[28] A. Burrows, E. Livne, L. Dessart, C. D. Ott, and J. Murphy, *A New Mechanism for Core-Collapse Supernova Explosions*, The Astrophysical Journal 640, pp. 878–890, (2006).

[29] Varun Srivastava et al., *Detection prospects of core-collapse supernovae with supernova-optimized third-generation gravitational-wave detectors*, Physical Review D 100, p. 043026, (2019).

[30] E. Cappellaro et al., *The rate of supernovae. II. The selection effects and the frequencies per unit blue luminosity.* Astronomy and Astrophysics 273, pp. 383–392, (1993).

[31] Jade Powell and Bernhard Müller, *Gravitational wave emission from 3D explosion models of core-collapse supernovae with low and normal explosion energies*, Monthly Notices of the Royal Astronomical Society 487, pp. 1178–1190, (2019).

[32] Jade Powell and Bernhard Müller, *Three-dimensional core-collapse supernova simulations of massive and rotating progenitors*, Monthly Notices of the Royal Astronomical Society 494, pp. 4665–4675, (2020).

[33] Anthony Mezzacappa et al., *Gravitational-wave signal of a core-collapse supernova explosion of a 15 $M_\odot$ star*, Physical Review D 102, p. 023027, (2020).

[34] David Radice, Viktoriya Morozova, Adam Burrows, David Vartanyan, and Hiroki Nagakura, *Characterizing the Gravitational Wave Signal from Core-collapse Supernovae*, The Astrophysical Journal 876, p. L9, (2019).

[35] Jade Powell, Bernhard Mueller, David R. Aguilera-Dena, and Norbert Langer, *Three dimensional magnetorotational core-collapse supernova explosions of a 39 solar mass progenitor star*, arXiv:2212.00200v1, (2022).

[36] M. Obergaulinger and M. Á. Aloy, *Magnetorotational core collapse of possible GRB progenitors. IV. A wider range of progenitors*, (2021).

[37] Viktoriya Morozova, David Radice, Adam Burrows, and David Vartanyan, *The Gravitational Wave Signal from Core-collapse Supernovae*, The Astrophysical Journal 861.1, p. 10, (2018).

[38] Alberto Iess, Elena Cuoco, Filip Morawski, and Jade Powell, *Core-Collapse supernova gravitational-wave search and deep learning classification*, Machine Learning: Science and Technology 1.2, p. 025014, (2020).

[39] Elena Cuoco et al., *On-line power spectra identification and whitening for the noise in interferometric gravitational wave detectors*, Classical and Quantum Gravity 18.9, p. 1727, (2001).

[40] P. Welch, *The use of fast Fourier transform for the estimation of power spectra: A method based on time averaging over short, modified periodograms*, IEEE Transactions on Audio and Electroacoustics 15, pp. 70–73, (1967).

[41] David L Donoho and Iain M Johnstone, *Ideal spatial adaptation by wavelet shrinkage*, Biometrika 81.3, pp. 425–455, (1994).